Improved pseudopotential lattice Boltzmann model for liquid water transport inside gas diffusion layers

Jiapei Yang[a], Linlin Fei[b], Xiaoqing Zhang[a], Xiao Ma[a,*], Kai H. Luo[c], Shijin Shuai[a]

[a] *State Key Laboratory of Automotive Safety and Energy, School of Vehicle and Mobility, Tsinghua University, Beijing 100084, China*
[b] *Center for Combustion Energy, Key Laboratory for Thermal Science and Power Engineering of Ministry of Education, Department of Energy and Power Engineering, Tsinghua University, Beijing 100084, China*
[c] *Department of Mechanical Engineering, University College London, Torrington Place, London WC1E 7JE, UK*

Abstract

Liquid water transport inside the gas diffusion layers (GDLs) plays a vital role in water management of proton exchange membrane fuel cells (PEMFCs). In this study, an improved pseudopotential multiphase lattice Boltzmann model is firstly developed to realize the actual density and viscosity ratios in porous media. The proposed model is based on a non-orthogonal multiple-relaxation-time (MRT) LB model and a new improved wettability boundary condition. In terms of the relationship between capillary pressure P_c and saturation s, the proposed model shows a good agreement with the experimental data. Using the validated model, the effects of capillary pres-

*Corresponding author.
Email address: max@tsinghua.edu.cn (Xiao Ma)

sures and contact angles of mixed wettability on the liquid water invasion process for Toray-090 GDLs with two Polytetrafluoroethylene (PTFE) contents (10 wt% and 20 wt%) are studied. It is found that the liquid water shows capillary fingering behaviors and the liquid water saturation profiles along the through-plane direction of the GDLs become more non-uniform with increasing contact angle of PTFE.
Keywords: Lattice Boltzmann method, Fuel cell, Gas diffusion layers, Liquid water transport, Large density ratio

1. Introduction

Proton exchange membrane fuel cells (PEMFCs) are known as one of the most promising power sources due to their high efficiency, low operating temperature and zero pollution emission [1, 2]. To make PEMFCs suitable for commercialization, a key issue to be resolved is internal water management that plays an important role in the performance and durability [3, 4, 5, 6]. The gas diffusion layers (GDLs) provide a transmission path for liquid water from the catalyst layers (CLs) and for the reactant from the gas channel to CLs [7, 8, 9]. Therefore the fundamental understanding of the liquid water transport process inside GDLs is essential for improving the effectiveness of water removal, which is the key purpose of any water management strategy for PEMFCs [10, 11, 12, 13, 14, 15, 16, 17, 18, 19].

Several research groups have conducted experiments to measure the relationship between the capillary pressure P_c (defined by the pressure difference

between the liquid phase and gas phase) and the water saturation s of the whole GDLs. In 2006, Gostick et al. [20] firstly attempted to obtain P_c vs. s curves through method of standard porosimetry (MSP). Then, Gostick et al. [21, 22] proposed a straightforward and accurate method, which increased the capillary pressure step by step and measured the water saturation with every step. The GDLs made by Toray and SGL were both studied with varying thickness, compression and Polytetrafluoroethylene (PTFE) loading. Their results confirmed the significant capillary pressure hysteresis. Harkness et al. [23] described a novel water porosimeter, which kept constant water injection rate in order to adjust the compression of GDL samples. The capillary pressure curves with varying compression and surface contact angle were obtained for samples with different compression and surface treatment, which showed that the imbibition process of water depended on surface contact angle. A micro-fluidic device developed by Fairweather et al. [24] was utilized by Hao and Cheng [25] to determine the capillary pressure of GDLs. A modified Leverett J-function with proper parameters was obtained based on their experimental results.

Owning to the complex mesoscopic-scale and anisotropic porous structure and two-phase flows, the detailed water transport process inside GDLs can not be directly measured in experiments. Recently, numerical simulations are used more and more widely to study this problem. Niu et al. [26, 27] adopted a two-phase volume of fluid (VOF) model to investigate the two-phase flow inside GDLs and liquid water distribution along the thickness

direction under different porosities and spatial wettability distributions. In their simulation, they found that the consideration of non-uniform porosity and mixed wettability were essential to concur well with the experimental observations. A pore-network model (PNM) was implemented by Sinha and Wang [28] to study liquid water transport through GDLs under different GDL wettability distributions.

Due to its kinetic nature and flexibility for complex boundary geometries, the lattice Boltzmann (LB) method is considered as a promising simulation tool for complex fluid flows [29, 30, 31, 32, 33, 34, 35, 36]. In the existing literature, the multiphase LB models can be divided into four categories: the color-gradient LB model [37], the pseudopotential LB model [38, 39], the free-energy LB model [40], and the phase-field LB model [41]. Hao and Cheng [42] studied the influence of uniform and non-uniform wettability distributions on liquid water transport inside GDLs by means of the free-energy multiphase LB model. The effects of GDL wettability and liquid water droplet size were investigated by Molaeimanesh and Akbari [43] via 3D single relaxation time (SRT) pseudopotential LB model. Chen and Jiang [44] used a free-energy LB model to investigate the PTFE content and distribution effects on the liquid water removal and relative permeability. Although the PTFE was non-uniformly distributed on the fibers' surface, the through-plane distribution of PTFE was an artificial setting. A similar study could also be found in the pseudopotential multiphase LB simulation by Yu et al. [45], who simulated the liquid water flowing through GDLs with different PTFE contents. It was

demonstrated that water's breakthrough times depended on the content and through-plane distribution of PTFE. Deng et al. [46] developed a stochastic model of microstructure of GDLs and micro porous layers (MPLs) and employed a pseudopotential LB model to analyse water transport dynamics within GDLs/MPLs and at the interfacial surface after comparing to X-ray tomographic microscopy experiment [47] and VOF results [26].

It is noted that in these studies based on LB simulations mentioned above, density and viscosity ratios of water-air system are ignored and are both artificially set to be 1.0. On one hand, the unity density and viscosity ratios could be attributed to the absence of a suitable pseudopotential multiphase LB model to account for high density and/or viscosity ratio with complex porous media. On the one hand, the typical operating condition of PEMFC falls into the regime of capillary fingering in the phase diagram [48] of the capillary number Ca vs. the viscosity ratio M, which means that the liquid water transport is mainly controlled by the capillary force [49]. However, the phase diagram by Lenormand et al. [48] aimed to be suitable for general porous media rather than specially for the GDLs with carbon fibers.

Free-energy LB models for porous media with large density ratios have been proposed in [50, 51, 52]. Niu et al. [50] ran a simulation by a free-energy LB model with large density ratios to study the water-gas transport processes in GDLs. Tabe et al. [51] developed a free-energy LB model with an improved Poisson equation solver to achieve large density differences in a porous medium. 2D liquid water behaviors in a gas channel and a sim-

plified GDL were demonstrated under different wettabilities. However, the computational cost for solving the Poisson equation remains huge. Later on, Sakaida et al. [52] used the free-energy LB model of [51] to determine the influence of the density ratio on the simulation results.

To the best of our knowledge, the pseudopotential LB model with high density ratio for multiphase flow in the GDLs of PEMFCs has not been proposed. To fill these voids, in this work, an improved multiphase lattice Boltzmann model is developed to realize the actual density and viscosity ratios in porous media. The proposed model is based on a non-orthogonal multiple-relaxation-time (MRT) LB model [53] and a new improved wettability boundary condition. Theoretical data is used to validate our simulation results. Moreover, our simulation results of P_c-s curves are compared with experimental and VOF-model results. Based on the validated model, the effects of pressures and contact angles of mixed wettability on the liquid water invasion process for two different actual porosity distributions of Toray-090 GDLs are studied.

2. Lattice Boltzmann model

In this section, the improved multiphase lattice Boltzmann model is presented. As in our previous work [54, 55], the D3Q19 MRT-LB model coupled with the pseudopotential LB model has been developed. In order to further enhance the numerical stability, reduce spurious current, and simplify the algorithm, the D3Q19 non-orthogonal MRT-LBM combined with the pseu-

dopotential model is adopted to simulate the actual water-air multiphase flows system [53].

In the present work, we focus on the isothermal two phase flow in the GDLs of PEMFCs where the heat pipe effect is not included. We would like to stress that our LB model could be easily extended to simulate thermal multiphase flow coupled with phase change process, as has been verified in our recent work [56].

2.1. The MRT-LB framework

The evolution equation of the particle distribution function f_i with MRT collision can be written as follows.

$$\begin{aligned} f_i\left(\mathbf{x}+\mathbf{e}_i\Delta t, t+\Delta t\right) =& f_i(\mathbf{x},t) - \left(\mathbf{M^{-1}SM}\right)_{i,k}\left[f_k - f_k^{eq}\right]\Big|_{(x,t)} \\ &+ \left(\mathbf{I} - \frac{\left(\mathbf{M^{-1}SM}\right)_{i,k}}{2}\right)\bar{F}_i(\mathbf{x},t)\Delta t \end{aligned} \tag{1}$$

where $\mathbf{e}_i$ is the discrete velocity vector at the point $\mathbf{x}$ and time t, $\Delta t = 1$ lattice unit (lu) is the lattice time step, f_i^{eq} is the corresponding equilibrium particle distribution function, and $\mathbf{I}$ is a unit tensor matrix. The forcing terms $\bar{F}_i$ are given by [57]

$$\bar{F}_i = \bar{\omega}\left(|\mathbf{e}_i|^2\right)\left[\frac{\mathbf{e}_i - \mathbf{u}}{c_s^2} + \frac{\left(\mathbf{u}\cdot\mathbf{e}_i\right)\mathbf{e}_i}{c_s^4}\right]\cdot\mathbf{F} \tag{2}$$

where $\mathbf{u}$ is the macroscopic velocity of fluid, the weights in the D3Q19 lattice are $\bar{\omega}(0) = 1/3$, $\bar{\omega}(1) = 1/18$, and $\bar{\omega}(2) = 1/36$, the lattice sound speed is

$c_s = c/\sqrt{3}$, and $c = \Delta x/\Delta t$ is the lattice constant. $\Delta x = 1$ lu is the lattice spacing step.

With the help of the transformation matrix $\mathbf{M}$, the distribution functions f_i and f_i^{eq} and the forcing terms $\bar{F}_i$ in physical space can be mapped onto the moment space. Thus if we define $\mathbf{m} = \mathbf{M}\mathbf{f}$, $\mathbf{m}^{eq} = \mathbf{M}\mathbf{f}^{eq}$, and $\widetilde{\mathbf{F}} = \mathbf{M}\overline{\mathbf{F}}$ then the collision step in the right side of Eq. (1) can be rewritten as the form

$$\mathbf{m}^* = \mathbf{m} - \mathbf{S}\left(\mathbf{m} - \mathbf{m}^{eq}\right) + \left(\mathbf{I} - \frac{\mathbf{S}}{2}\right)\Delta t\widetilde{\mathbf{F}} \tag{3}$$

Then the streaming process is given as

$$f_i\left(\mathbf{x} + \mathbf{e}_i\Delta t, t + \Delta t\right) = f_i^*(\mathbf{x}, t) \tag{4}$$

where $\mathbf{f}^* = \mathbf{M}^{-1}\mathbf{m}^*$.

The macroscopic density and velocity can be obtained by

$$\rho = \sum_i f_i, \quad \rho\mathbf{u} = \sum_i f_i\mathbf{e}_i + \frac{\Delta t\mathbf{F}}{2} \tag{5}$$

2.2. The non-orthogonal MRT model

A D3Q19 non-orthogonal MRT collision operator is now presented. The raw moment set $\mathbf{m} = [m_0, m_1, \ldots, m_{18}]^{\mathrm{T}}$ is adopted [31]:

$$\begin{aligned}\mathbf{m} = [&k_{000}, k_{100}, k_{010}, k_{001}, k_{110}, k_{101}, k_{011}, k_{200} + k_{020} + k_{002}, k_{200} - k_{020},\\ &k_{200} - k_{002}, k_{120}, k_{102}, k_{210}, k_{201}, k_{012}, k_{021}, k_{220}, k_{202}, k_{022}]^{\mathrm{T}}\end{aligned} \tag{6}$$

where k_{mnp} is the moment of the particle distribution function f_i [53]

$$k_{mnp} = \left\langle f_i | e_{ix}^m e_{iy}^n e_{iz}^p \right\rangle \tag{7}$$

The diagonal relaxation matrix $\mathbf{S}$ reads

$$\mathbf{S} = \mathrm{diag}\left(s_0, s_1, s_1, s_1, s_v, s_v, s_v, s_b, s_v, s_v, s_3, s_3, s_3, s_3, s_3, s_3, s_4, s_4, s_4\right) \tag{8}$$

where relaxation factors s_v and s_b are related to the kinematic and bulk viscosities through $\nu = \left(1/s_v - 1/2\right) c_s^2 \Delta t$ and $\xi = 2/3 \left(1/s_b - 0.5\right) c_s^2 \Delta t$. In this work, we set $\nu_{\mathrm{l}} = 0.01$ and $\nu_{\mathrm{g}} = 0.1497$ for liquid water and air, respectively, which correspond to the actual kinematic viscosity ratio (1:14.97) for the water-air system at 20 °C.

The D3Q19 transformation matrix $\mathbf{M}$, equilibrium raw moments $\mathbf{m}^{eq} = [m_0^{eq}, m_1^{eq}, \ldots, m_{18}^{eq}]$, and the forcing terms $\tilde{\mathbf{F}} = \left[\tilde{F}_0, \tilde{F}_1, \ldots, \tilde{F}_{18}\right]$ are given,

respectively,

$$\mathbf{M} = \left[\begin{array}{cccccccccccccccccc}
1 & 1 & 1 & 1 & 1 & 1 & 1 & 1 & 1 & 1 & 1 & 1 & 1 & 1 & 1 & 1 & 1 & 1 & 1 \\
0 & 1 & -1 & 0 & 0 & 0 & 0 & 1 & -1 & 1 & -1 & 1 & -1 & 1 & -1 & 0 & 0 & 0 & 0 \\
0 & 0 & 0 & 1 & -1 & 0 & 0 & 1 & 1 & -1 & -1 & 0 & 0 & 0 & 0 & 1 & -1 & 1 & -1 \\
0 & 0 & 0 & 0 & 0 & 1 & -1 & 0 & 0 & 0 & 0 & 1 & 1 & -1 & -1 & 1 & 1 & -1 & -1 \\
0 & 0 & 0 & 0 & 0 & 0 & 0 & 1 & -1 & -1 & 1 & 0 & 0 & 0 & 0 & 0 & 0 & 0 & 0 \\
0 & 0 & 0 & 0 & 0 & 0 & 0 & 0 & 0 & 0 & 0 & 1 & -1 & -1 & 1 & 0 & 0 & 0 & 0 \\
0 & 0 & 0 & 0 & 0 & 0 & 0 & 0 & 0 & 0 & 0 & 0 & 0 & 0 & 0 & 1 & -1 & -1 & 1 \\
0 & 1 & 1 & 1 & 1 & 1 & 1 & 2 & 2 & 2 & 2 & 2 & 2 & 2 & 2 & 2 & 2 & 2 & 2 \\
0 & 1 & 1 & -1 & -1 & 0 & 0 & 0 & 0 & 0 & 0 & 1 & 1 & 1 & 1 & -1 & -1 & -1 & -1 \\
0 & 1 & 1 & 0 & 0 & -1 & -1 & 1 & 1 & 1 & 1 & 0 & 0 & 0 & 0 & -1 & -1 & -1 & -1 \\
0 & 0 & 0 & 0 & 0 & 0 & 0 & 1 & -1 & 1 & -1 & 0 & 0 & 0 & 0 & 0 & 0 & 0 & 0 \\
0 & 0 & 0 & 0 & 0 & 0 & 0 & 0 & 0 & 0 & 0 & 1 & -1 & 1 & -1 & 0 & 0 & 0 & 0 \\
0 & 0 & 0 & 0 & 0 & 0 & 0 & 1 & 1 & -1 & -1 & 0 & 0 & 0 & 0 & 0 & 0 & 0 & 0 \\
0 & 0 & 0 & 0 & 0 & 0 & 0 & 0 & 0 & 0 & 0 & 1 & 1 & -1 & -1 & 0 & 0 & 0 & 0 \\
0 & 0 & 0 & 0 & 0 & 0 & 0 & 0 & 0 & 0 & 0 & 0 & 0 & 0 & 0 & 1 & -1 & 1 & -1 \\
0 & 0 & 0 & 0 & 0 & 0 & 0 & 0 & 0 & 0 & 0 & 0 & 0 & 0 & 0 & 1 & 1 & -1 & -1 \\
0 & 0 & 0 & 0 & 0 & 0 & 0 & 1 & 1 & 1 & 1 & 0 & 0 & 0 & 0 & 0 & 0 & 0 & 0 \\
0 & 0 & 0 & 0 & 0 & 0 & 0 & 0 & 0 & 0 & 0 & 1 & 1 & 1 & 1 & 0 & 0 & 0 & 0 \\
0 & 0 & 0 & 0 & 0 & 0 & 0 & 0 & 0 & 0 & 0 & 0 & 0 & 0 & 0 & 1 & 1 & 1 & 1
\end{array}\right] \tag{9}$$

$$\begin{aligned}\mathbf{m}^{eq} = \big[&\rho, \rho u_x, \rho u_y, \rho u_z, \rho u_x u_y, \rho u_x u_z, \rho u_y u_z, \rho\left(1+\mathbf{u}^2\right), \rho\left(u_x^2-u_y^2\right), \\ &\rho\left(u_x^2-u_z^2\right), \rho c_s^2 u_x, \rho c_s^2 u_x, \rho c_s^2 u_y, \rho c_s^2 u_z, \rho c_s^2 u_y, \rho c_s^2 u_z, \\ &\rho c_s^2\left(c_s^2+u_x^2+u_y^2\right), \rho c_s^2\left(c_s^2+u_x^2+u_z^2\right), \rho c_s^2\left(c_s^2+u_y^2+u_z^2\right)\big]^{\mathrm{T}}\end{aligned} \tag{10}$$

$$\begin{aligned}\tilde{\mathbf{F}} = [&0, F_x, F_y, F_z, F_x u_y + F_y u_x, F_x u_z + F_z u_x, F_y u_z + F_z u_y, 2\mathbf{F}\cdot\mathbf{u}, \\ &2\left(F_x u_x - F_y u_y\right), 2\left(F_x u_x - F_z u_z\right), F_x c_s^2, F_x c_s^2, F_y c_s^2, F_z c_s^2, F_y c_s^2, \\ &F_z c_s^2, 2c_s^2\left(F_x u_x + F_y u_y\right), 2c_s^2\left(F_x u_x + F_z u_z\right), 2c_s^2\left(F_y u_y + F_z u_z\right)\big]^{\mathrm{T}}\end{aligned} \tag{11}$$

From the elements of M, it is noted that the number of non-zero elements is much smaller than the classical orthogonal MRT model [58], that is to say the calculation is simplified and the computational load is reduced. For the details of non-orthogonal MRT model, the interested readers are kindly directed to [59, 60, 53].

2.3. The pseudopotential multiphase model

In the pseudopotential multiphase model, the interaction force among fluid particles is defined as [38, 39]

$$\mathbf{F}_{\mathrm{int}} = -G\psi(\mathbf{x}) \sum_i w\left(|\mathbf{e}_i|^2\right) \psi\left(\mathbf{x} + \mathbf{e}_i \Delta t\right) \mathbf{e}_i \tag{12}$$

where $w\left(|\mathbf{e}_i|^2\right) = \bar{\omega}\left(|\mathbf{e}_i|^2\right)/c_s^2$ is the normalized weight, ψ is the pseudopotential that is give by [61]

$$\psi = \sqrt{2\left(p_{\mathrm{EOS}} - \rho c_s^2\right)/Gc^2} \tag{13}$$

where G is the interaction strength and usually equal to -1.0, p_{EOS} is the pressure determined by the equation of state (EOS). In this work, a piecewise linear EOS is adopted, as follows [62]:

$$p(\rho) = \begin{cases} \rho\theta_{\mathrm{v}}, \rho \leq \rho_1 \\ \rho_1\theta_{\mathrm{v}} + (\rho - \rho_1)\,\theta_{\mathrm{m}}, \quad \rho_1 \leq \rho \leq \rho_2 \\ \rho_1\theta_{\mathrm{v}} + (\rho_2 - \rho_1)\,\theta_{\mathrm{m}} + (\rho - \rho_2)\,\theta_{\mathrm{l}}, \quad \rho > \rho_2 \end{cases} \tag{14}$$

where θ_{v}, θ_{m} and θ_{l} are adjustable factors. Once they are fixed, the other unknown variables ρ_1 and ρ_2 can be obtained according to the liquid density ρ_{l} and vapour density ρ_{v}.

In order to characterize the realistic water-air system at around 20 °C, a large density ratio is fixed $\rho_{\mathrm{l}}/\rho_{\mathrm{v}} = 1000/1 = 1000$ in this study.

Furthermore, for the sake of simulating high density ratio multiphase flows with tunable surface tension, several terms in $\tilde{\mathbf{F}}$ should be improved, which is given by [31]

$$\begin{gathered} \tilde{F}_4' = \tilde{F}_4 - \frac{Q_{xy}}{\left(s_v^{-1}-0.5\right)\Delta t}, \tilde{F}_5' = \tilde{F}_5 - \frac{Q_{xz}}{\left(s_v^{-1}-0.5\right)\Delta t}, \tilde{F}_6' = \tilde{F}_6 - \frac{Q_{yz}}{\left(s_v^{-1}-0.5\right)\Delta t} \\ \tilde{F}_7' = \tilde{F}_7 + \frac{3\varepsilon|F_{int}|^2}{\psi^2\left(s_e^{-1}-0.5\right)\Delta t} + \frac{4(Q_{xx}+Q_{yy}+Q_{zz})}{5\left(s_e^{-1}-0.5\right)\Delta t} \\ \tilde{F}_8' = \tilde{F}_8 - \frac{(Q_{xx}-Q_{yy})}{\left(s_v^{-1}-0.5\right)\Delta t}, \\ \tilde{F}_9' = \tilde{F}_9 - \frac{(Q_{xx}-Q_{zz})}{\left(s_v^{-1}-0.5\right)\Delta t} \end{gathered} \tag{15}$$

where ε is an adjustable parameter to control the mechanical stability con-

dition. In this work, ε is fixed as 0.1. The tensor $\mathbf{Q}$ can be obtained from

$$\mathbf{Q} = \kappa \frac{\mathbf{G}}{\mathbf{2}} \psi(\mathbf{x}) \sum_{\mathbf{i}} \mathbf{w} \left(|\mathbf{e_i}|^{\mathbf{2}} \right) \left[\psi \left(\mathbf{x} + \mathbf{e_i} \boldsymbol{\Delta} \mathbf{t} \right) - \psi(\mathbf{x}) \right] \mathbf{e_i} \mathbf{e_i} \tag{16}$$

where κ is a parameter to linearly tune the surface tension.

2.4. Wettability boundary condition

In principle, the implementation of wettability boundary condition of GDL fibers is considered as a hard task as a result of complex porous structure. Here, a modified pseudopotential-based contact angle scheme proposed by Li et al. [63] is adopted. In this scheme, the pseudopotential-based fluid–solid interaction is given as follows:

$$\mathbf{F}_{\text{ads}}(\mathbf{x}) = -G_{\text{ads}} \psi(\mathbf{x}) \sum_{i} w \left(|\mathbf{e}_i|^2 \right) \psi(\mathbf{x}) s \left(\mathbf{x} + \mathbf{e}_i \Delta t \right) \mathbf{e}_i \tag{17}$$

where G_{ads} is the adjustment parameter of contact angle and the switch function $s\left(\mathbf{x} + \mathbf{e}_i \Delta t\right)$ equals 1 or 0 for a solid or a fluid node, respectively. It should be noted that the calculation of $\mathbf{F}_{\text{ads}}(\mathbf{x})$ for the fluid node adjacent to solid node does not need the density of solid node while the calculation of $\mathbf{F}_{\text{int}}(\mathbf{x})$ for the fluid node adjacent to solid node does need that. Thus a ghost layer of fluid near the solid boundary is necessary. In general, the information in the ghost layer is equal to the nearest fluid layer's for a planar surface. But this is difficult for an irregular geometry. Therefore, inspired by Li et al. [30], we propose that the density of node in the ghost layer is set to

be the weighted average density of the surrounding fluid nodes of the ghost node, i.e.

$$\rho_{\text{ghost}}(\mathbf{x}) = \frac{\sum_{\text{i}} \bar{\omega}_{\text{i}} \rho\left(\mathbf{x} + \mathbf{e}_i \Delta t\right)\left(1 - s\left(\mathbf{x} + \mathbf{e}_i \Delta t\right)\right)}{\sum_{\text{i}} \bar{\omega}_{\text{i}}\left(1 - s\left(\mathbf{x} + \mathbf{e}_i \Delta t\right)\right)} \tag{18}$$

The contact angle in the paper of Li et al. [30] is adjusted by virtual density in the ghost layer near a boundary. In contrast, the contact angle in our proposed model is still controlled by G_{abs}. And such implementation ensures that $G_{\text{abs}} < 0$, $G_{\text{abs}} = 0$, and $G_{\text{abs}} > 0$ realize the hydrophilic, neutral, and hydrophobic contact angles, respectively.

With the fluid–fluid interaction $\mathbf{F}_{\text{int}}$, the total force $\mathbf{F}$ in Eq. (2) is given by

$$\mathbf{F} = \mathbf{F}_{\text{int}} + \mathbf{F}_{\text{ads}} \tag{19}$$

3. Model validation

3.1. Contact angle test

The wettability boundary condition proposed in section 2.4 is validated by simulating an equilibrium droplet on a flat surface with a radius of 30 in a $200 \times 200 \times 100$ mesh. The wettability boundary condition and bounce-back boundary condition are applied at the bottom flat surface of the computational domain. Periodic boundary conditions are employed at the other boundary. Figure 1 shows the different static contact angles via changing the adjustment parameter G_{abs}. According to Fig. 1, the expected contact angle can be obtained by setting the corresponding G_{abs}.

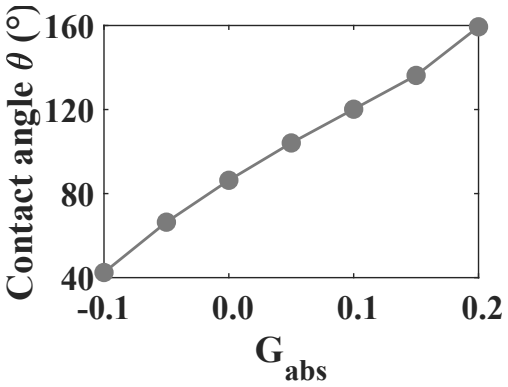

Figure 1: The relationship between the static contact angles of a liquid droplet on a flat surface and the adjustment parameter G_{abs}.

3.2. Liquid water invasion through a perforated plate

The simulation of liquid water invasion process through a perforated plate is adopted to validate the multiphase model and obtain the surface tension in the LBM framework, which is similar to Hao and Cheng [42]. Here, we consider a rectangle computational domain of 60×50 mesh. Figure 2(a)-(d) depicts the evolution process of breaking through perforated plate (with five different width pores of 3, 5, 11, 5, and 3 spacings, respectively) for the contact angle of $\theta = 130°$. The bottom boundary is the inlet velocity boundary condition of 1.0×10^{-4}, which corresponds to the capillary number of 1.333×10^{-4}.

According to the Laplace's law, the capillary pressure P_c and interface curvature radius r_c should satisfy:

$$P_c = \frac{\sigma}{r_c} \tag{20}$$

where $r_c = R/cos(\pi - \theta)$, R is the radius of largest pore.

The relationship between P_c/σ and curvature $1/r_c$ is illustrated in Fig. 2(e). It is obvious that the LB results agree well with the analytical results. In addition, the surface tension $\sigma = 7.5$ is obtained from the slope of the line.

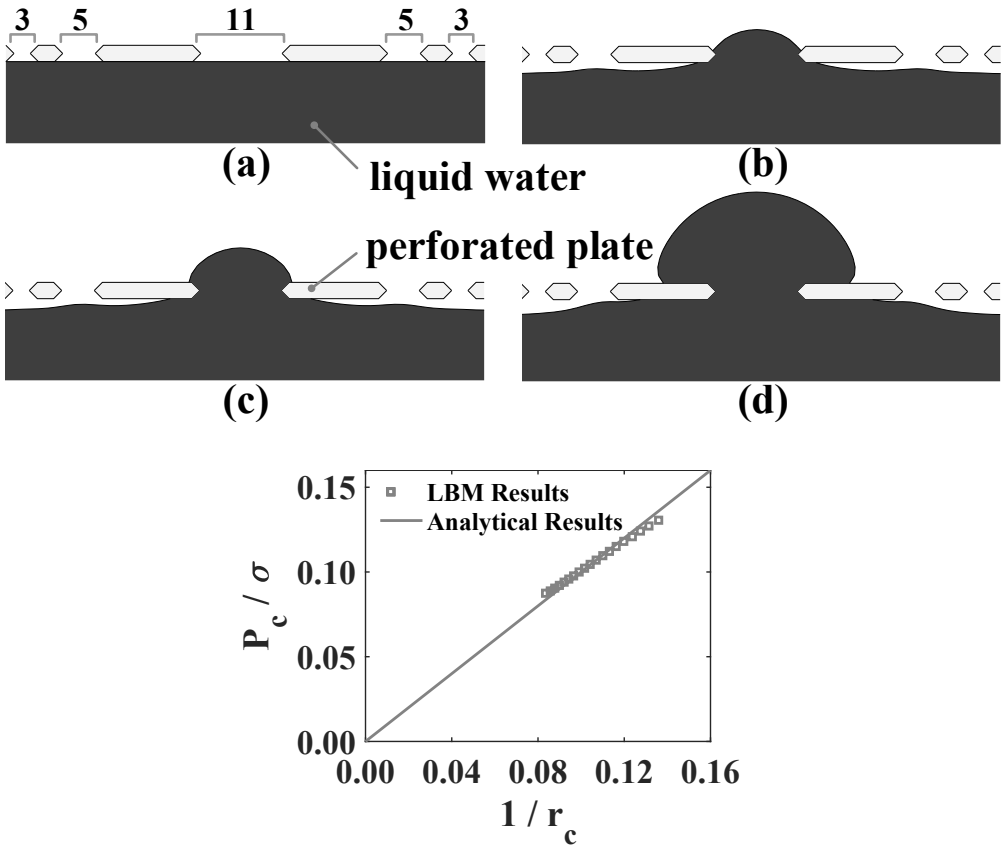

(e)

Figure 2: (a)-(d) The liquid water (blue area) invasion process through a perforated plate (yellow area) for contact angle of 130° and the capillary number of 1.333×10^{-4}; (e) The relationship between P_c/σ and the curvature radius r_c.

4. Simulation setups

4.1. Reconstructed model and computational domain

Toray-090 carbon paper is composed of carbon fibers, and usually coated with PTFE to enhance hydrophobicity. And the binders are ignored to simplify the reconstruction in this model. The typical fiber diameter is in the range of 7–10 μm [64, 65]. Here, the diameter of Toray-090 GDLs is fixed to 7.0 μm. Based on the GDL stochastic reconstruction method in our previous study [55], the Toray-090 GDLs with specified PTFE content is firstly generated. After that, the points at the surfaces of generated structures are randomly selected to be PTFE locations until the specified PTFE content is achieved. Figure 3(a) shows the reconstructed Toray-090 GDLs with PTFE locations. In addition to reconstructed GDLs, the computational domain also includes a buffer zone (40 spacings) at the top of GDLs and a reservoir zone (10 spacings) at the bottom of GDLs to provide access to liquid water. In this study, the distributions of local porosity along the through-plane direction of Ref. [66, 27] are adopted to reconstruct GDLs with different PTFE contents (0 wt%, 10 wt%, 20 wt%), as shown in Fig. 3(b).

4.2. Unit conversion

In LB simulations, the variables are operated in the lattice unit system. Thus it is necessary to convert the LB unit system to the physical unit system so that the experimental results can be used to verify the simulation results. Here we focus on two important scale conversions: length scale

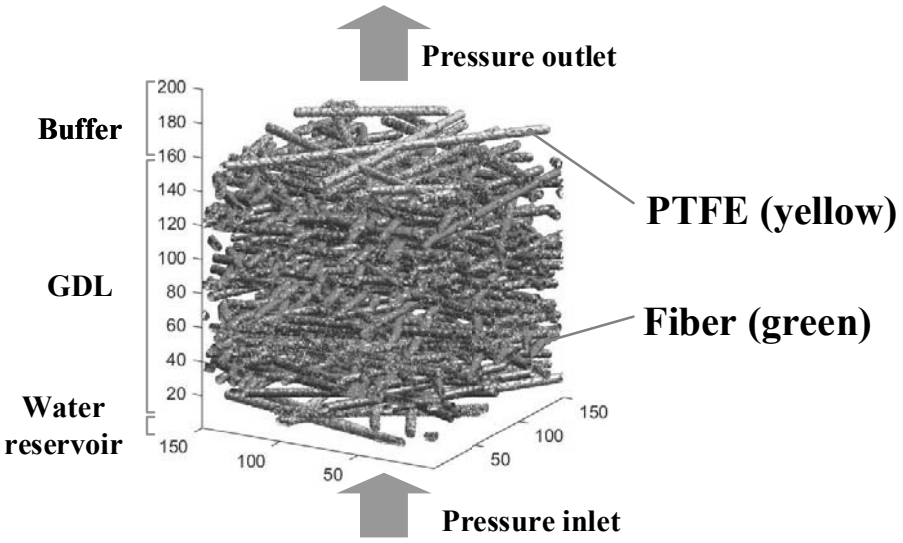

(a)

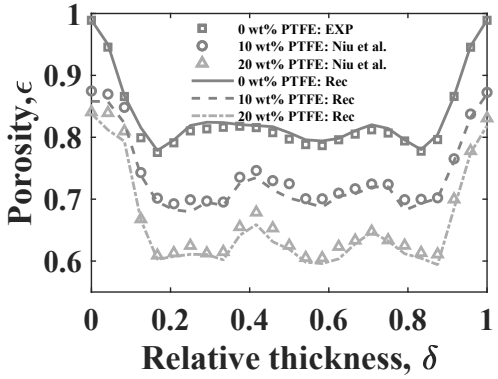

(b)

Figure 3: (a) Reconstructed Toray-090 GDLs with PTFE locations and computational domain; (b) The comparisons of reconstructed, experimental [66], and literature [27] local porosity distribution results along the through-plane direction for GDLs with different PTFE contents (0 wt%, 10 wt%, 20 wt%)

C_{L} and pressure scale C_{P}. A room-temperature ($\sim 20\ ^{\circ}C$) experiment [22] is adopted to validate the LB model. At $20^{\circ}C$, water density, kinematic

viscosity and surface tension are, respectively, $\rho_{\mathrm{w,P}} = 998.2\ \mathrm{kg \cdot m^{-3}}$, $\nu_{\mathrm{w,P}} = 1.01 \times 10^{-6}\ \mathrm{m^2 \cdot s^{-1}}$, and $\sigma_{\mathrm{w,P}} = 0.07269\ \mathrm{N \cdot m^{-1}}$, where subscript w is the water property and subscript P is the physical system. At the same temperature as water, air density and kinematic viscosity are $\rho_{\mathrm{a,P}} = 1.205\ \mathrm{kg \cdot m^{-3}}$ and $\nu_{\mathrm{a,P}} = 1.51 \times 10^{-5}\ \mathrm{m^2 \cdot s^{-1}}$, respectively, where subscript a is the air property.

1) Determine the characteristic length of GDLs. In general, the fiber diameter is chosen as the characteristic length of GDLs. The fiber diameter of Toray-090 GDLs is 7.0 μm [42] while the average fiber diameter of the reconstructed GDLs is set to be 3.9 lattice for 10 wt% and 3.5 lattice for 20 wt%. Thus the length scale is $C_{\mathrm{L}} = 1.8$ μm for 10 wt% and 2.0μm lattice for 20 wt%.

2) Compute the pressure scale. The pressure scale is derived from two non-dimensional numbers: Euler number ($\mathrm{Eu} = \mathrm{P}/\rho u^2$) and Weber number ($We = \rho u^2 L/\sigma$) [46]. In order to match the two non-dimensional numbers simultaneously for the LB system and the physical system, multiply Euler number by Weber number to cancel out the term of ρu^2. Then the pressure scale is $C_{\mathrm{P}} = \sigma_{\mathrm{w,P}} / \left(C_{\mathrm{L}} \sigma_{\mathrm{w,LB}}\right) = 5.4 \times 10^3 \mathrm{Pa}$ for 10 wt% and 4.8×10^3 Pa for 20 wt%.

3) Determine the density and viscosity ratios: $\rho_{\mathrm{w,P}}/\rho_{\mathrm{a,P}} \approx 1000 = \rho_{\mathrm{w,LB}}/\rho_{\mathrm{a,LB}}$ and $\nu_{\mathrm{a,P}}/\nu_{\mathrm{w,P}} \approx 14.97 = \nu_{\mathrm{a,LB}}/\nu_{\mathrm{w,LB}}$.

4.3. Mesh independence

Before the final simulations, the mesh number effect on the curve of $P_c - s$ is conducted to obtain a mesh-independent result. In order to reduce computational load, the porosity distribution of Toray-090 with 0 wt% PTFE is adopted and the uniform contact angle is set to be a fixed value of 125°. Four different mesh sizes of 0.5, 2.0, 4.5 and 8.0 million are investigated. Figure 4 presents the comparison of curves of $P_c - s$ for four different mesh sizes. This indicates that the mesh size of 4.5 million does not show significant differences comparing to the mesh size of 8.0 million. Thus, in the following study, the mesh size of 4.5 million ($150 \times 150 \times 200$) is enough and used for the simulation.

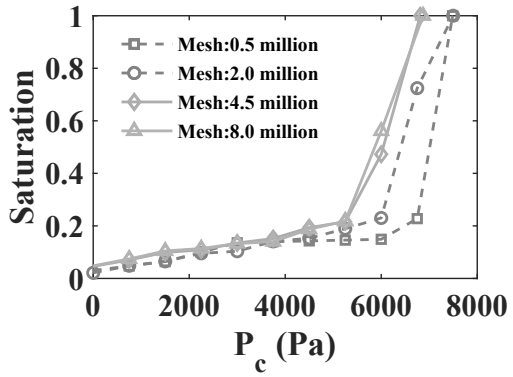

Figure 4: The comparison of curves of $P_c - s$ with four different mesh sizes.

5. Results and discussion

In this section, the liquid water invasion processes with varying PTFE contents (10 wt%, 20 wt%), pressures, and wettability are studied to reveal

the influence of density and viscosity ratios. In the follow text, the non-uniform wettability of 95° for carbon fiber and 125° for pure PTFE is assumed for Toray-090 GDLs.

5.1. Influences of pressures and PTFE contents on liquid water invasion process

Figure 5 presents the results of the $P_c - s$ curves with two PTFE contents: (a) 10 wt% PTFE and (b) 20 wt% PTFE. Under the 10 wt% PTFE content, the results of experiment [25], VOF [27], and free-energy LBM [25] are also plotted together with our simulation results in Fig. 5(a). It is found that the saturation increases slowly with capillary pressure until 4000 Pa. And then there is a dramatic increase of $P_c - s$ curves when capillary pressure is larger than 4000 Pa.. This suggests that the liquid water can break through the GDLs in this range of capillary pressure, which exhibits good agreement with the range of capillary pressure in [67]. Finally, as the capillary pressure continues to increase, the GDLs is close to be fully saturated. It is obvious that the $P_c - s$ curves of our LBM results can predict the experimental and VOF results well unlike the free-energy LBM results. In addition, Fig. 5(b) shows the comparative results of our simulation, experiment [22], and VOF [27] with 20 wt% PTFE content. Due to the more hydrophobic and small pores in the GDLs of 20 wt% PTFE content, the breakthrough pressure increases to 6000 Pa. The LBM results also agree well with experimental and VOF results. In addition, it should be noted that ignoring the binders

in the reconstructed GDLs may result in the small deviation of $P_c - s$ curves at middle area compared to the experimental data [68].

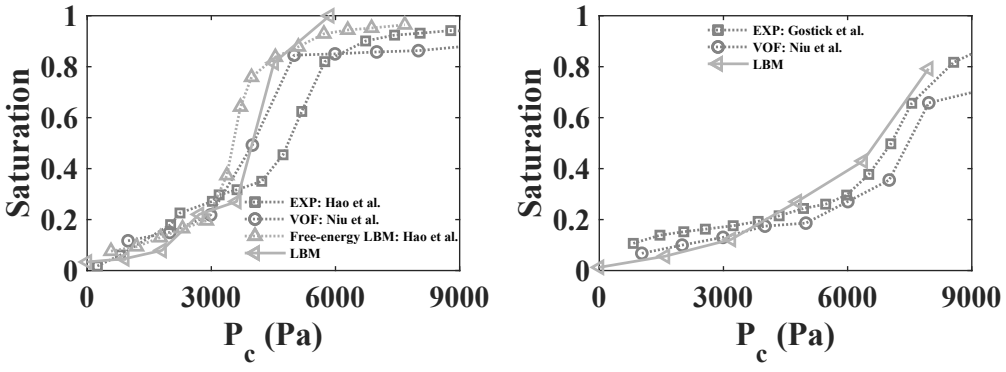

(a) 10 wt% PTFE content (b) 20 wt% PTFE content

Figure 5: Comparison of $P_c - s$ curves of LBM simulation results with experiment [22, 25], VOF [27], and free-energy LBM results [25] with two PTFE contents: (a) 10 wt% PTFE content; (b) 20 wt% PTFE content.

Comparison of liquid water saturation distributions along the through-plane direction of the GDLs under different capillary pressures is presented in Fig. 6. Figure 6(a) shows the liquid water saturation distributions inside GDLs with 10 wt% PTFE content under 1000 Pa, 3000 Pa, and 5000 Pa while Fig. 6(b) presents the liquid water saturation distributions inside GDLs with 20 wt% PTFE content under 1709 Pa, 5128 Pa, and 8547 Pa. It is shown that the liquid water saturation distributions under different capillary pressures are approximately concave shapes and similar with each other.

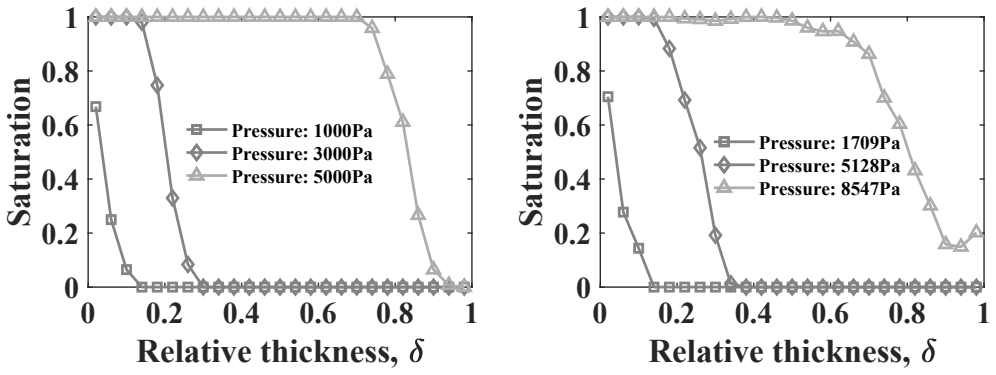

(a) 10 wt% PTFE content (b) 20 wt% PTFE content

Figure 6: Comparison of liquid water saturation distributions along the through-plane direction of the GDLs under different capillary pressures with two PTFE contents: (a) 10 wt% PTFE content; (b) 20 wt% PTFE content.

5.2. Influences of wettability and PTFE contents on liquid water invasion process

Figure 7 shows the typical snapshots of time evolution of liquid water transport inside GDLs with varying wettability and contents of PTFE (95°, 125°, 140°) and the unchanged wettability of fiber (95°). According to these figures, we can obtain the liquid water saturations in the whole GDLs and liquid water saturation distributions along the through-plane direction of the GDLs at the breakthrough time or final steady time, which are shown in Fig. 8(a) and Fig. 8(b)(c), respectively. In order to show the water invasion process in the whole GDLs as clear as possible, the capillary pressure with 10 wt% PTFE content is set to be 5000 Pa while the capillary pressure with 20 wt% PTFE content is set to be 8500 Pa.

From the view of wettability, it is found from Fig. 8(a) that the liquid

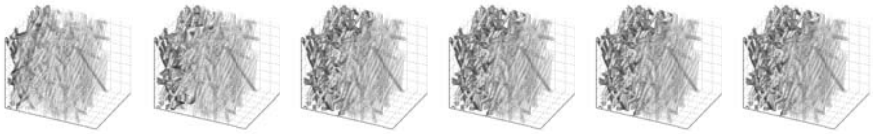

(a) CA:95°/95°, 10 wt% PTFE content

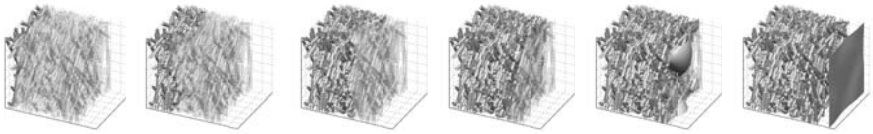

(b) CA:95°/95°, 20 wt% PTFE content

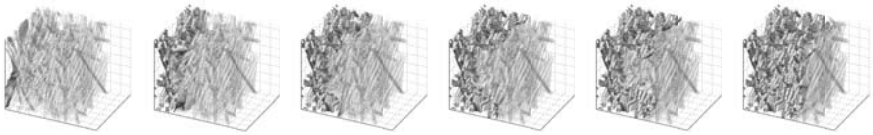

(c) CA:95°/125°, 10 wt% PTFE content

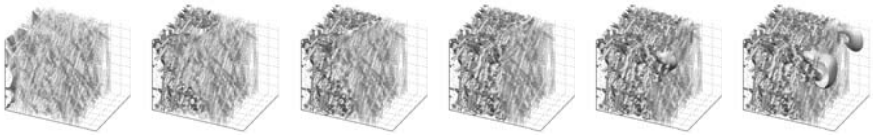

(d) CA:95°/125°, 20 wt% PTFE content

Figure 7: The typical snapshots of time evolution of liquid water transport inside GDLs with varying wettability and contents of PTFE (95°, 125°, 140°)and the unchanged wettability of fiber (95°).

water saturation in the whole GDLs decreases with increasing contact angle of PTFE. A larger contact angle of PTFE increases the hydrophobicity of GDLs, leading to larger capillary resistance in the liquid water transport process inside GDLs. The liquid water needs to enter into the relatively larger pores to invade through the GDLs if the PTFE is more hydrophobic. Thus the liquid water shows capillary fingering behaviors and the liquid water sat-

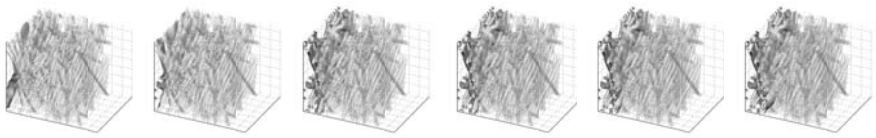

(e) CA:95°/140°, 10 wt% PTFE content

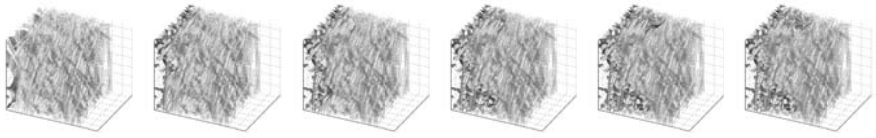

(f) CA:95°/140°, 20 wt% PTFE content

Figure 7: (continued)

uration distributions along the through-plane direction of the GDLs become more non-uniform with increasing contact angle of PTFE, as shown in Figs. 7 and 8(b)(c), respectively.

Comparing the results of PTFE contents of 10 wt% and 20 wt%, the liquid water saturations in the whole GDLs (Fig. 8(a)) are not affected much by PTFE content while the liquid water saturation distributions (Figs. 7 and 8(b)(c)) are affected significantly by PTFE content. This may be explained by the fact that the hydrophilic pores still exist in many regions of GDLs while the distributions of hydrophilic pores are changed owning to randomness with the increase of PTFE content. These results are in agreement with those obtained by Hao and Cheng [25].

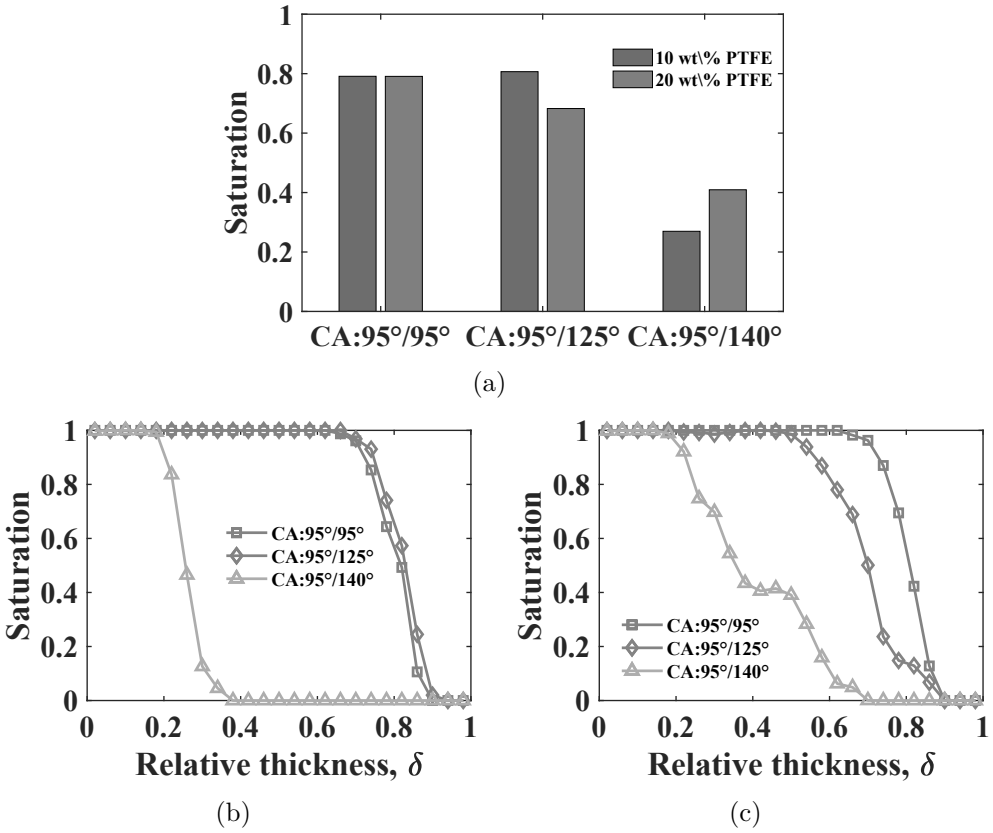

(a) (b) (c)

Figure 8: (a) The liquid water saturations in the whole GDLs for different mixed wettability with two PTFE contents at the breakthrough time or final steady time. Comparison of liquid water saturation distributions along the through-plane direction of the GDLs for different mixed wettability with two PTFE contents at the breakthrough time or final steady time: (b) 10 wt% PTFE content; (c) 20 wt% PTFE content.

6. Conclusion

In summary, an improved pseudopotential lattice Boltzmann model is firstly developed, which can realize the actual density and viscosity ratios in porous media. In this model, a non-orthogonal multiple-relaxation-time (MRT) LB model and a new improved wettability boundary condition are incorporated into the pseudopotential multiphase model. The P_c-s curves

of the proposed model results are compared with experiment and show a good agreement with experimental data. In addition, the effects of capillary pressures and contact angles of mixed wettability on the liquid water invasion process for Toray-090 GDLs with two PTFE contents (10 wt% and 20 wt%) are studied. The obtained results lead to the conclusion that the liquid water saturation distributions under different capillary pressures are approximately concave shapes and similar to each other. The liquid water shows capillary fingering behaviors and the liquid water saturation profiles along the through-plane direction of the GDLs become more non-uniform with increasing contact angle of PTFE.

7. Acknowledgement

This research is supported by the Beijing Municipal Science & Technology Commission (Grant No. Z181100004518004), the National Key R&D Program of China (Integration and Control of Fuel Cell Engine for Heavy Duty Truck & Assessment Technologies of Fuel Cell Engine Reliability for Heavy Duty Truck), and the National Key R&D Program of China (Grant No. 2018YFB0105403). Supercomputing time on ARCHER is provided by the "UK Consortium on Mesoscale Engineering Sciences (UKCOMES)" under the UK Engineering and Physical Sciences Research Council (Grant No. EP/R029598/1).

References

[1] Y. Wang, D. F. R. Diaz, K. S. Chen, Z. Wang, X. C. Adroher, Materials, technological status, and fundamentals of pem fuel cells–a review, Materials Today (2019).

[2] S. J. Peighambardoust, S. Rowshanzamir, M. Amjadi, Review of the proton exchange membranes for fuel cell applications, International journal of hydrogen energy 35 (2010) 9349–9384.

[3] K. Jiao, X. Li, Water transport in polymer electrolyte membrane fuel cells, Progress in energy and combustion Science 37 (2011) 221–291.

[4] M. Andersson, S. Beale, M. Espinoza, Z. Wu, W. Lehnert, A review of cell-scale multiphase flow modeling, including water management, in polymer electrolyte fuel cells, Applied Energy 180 (2016) 757–778.

[5] S. G. Kandlikar, E. J. See, M. Koz, P. Gopalan, R. Banerjee, Two-phase flow in gdl and reactant channels of a proton exchange membrane fuel cell, international journal of hydrogen energy 39 (2014) 6620–6636.

[6] A. Bazylak, Liquid water visualization in pem fuel cells: A review, International journal of hydrogen energy 34 (2009) 3845–3857.

[7] J. Park, H. Oh, T. Ha, Y. I. Lee, K. Min, A review of the gas diffusion layer in proton exchange membrane fuel cells: durability and degradation, Applied Energy 155 (2015) 866–880.

[8] X. Zhou, Z. Niu, Y. Li, X. Sun, Q. Du, J. Xuan, K. Jiao, Investigation of two-phase flow in the compressed gas diffusion layer microstructures, International Journal of Hydrogen Energy 44 (2019) 26498–26516.

[9] M. Espinoza-Andaluz, M. Andersson, B. Sundén, Comparing through-plane diffusibility correlations in pefc gas diffusion layers using the lattice boltzmann method, International Journal of Hydrogen Energy 42 (2017) 11689–11698.

[10] R. Omrani, B. Shabani, Gas diffusion layer modifications and treatments for improving the performance of proton exchange membrane fuel cells and electrolysers: A review, International Journal of Hydrogen Energy 42 (2017) 28515–28536.

[11] S. Park, J.-W. Lee, B. N. Popov, A review of gas diffusion layer in pem fuel cells: Materials and designs, International Journal of Hydrogen Energy 37 (2012) 5850–5865.

[12] J. P. Owejan, T. Trabold, D. Jacobson, M. Arif, S. Kandlikar, Effects of flow field and diffusion layer properties on water accumulation in a pem fuel cell, in: International Conference on Nanochannels, Microchannels, and Minichannels, volume 4272, 2007, pp. 311–320.

[13] M. E. A. B. Amara, S. B. Nasrallah, Numerical simulation of droplet dynamics in a proton exchange membrane (pemfc) fuel cell micro-channel, International journal of hydrogen energy 40 (2015) 1333–1342.

[14] J. P. Owejan, J. J. Gagliardo, J. M. Sergi, S. G. Kandlikar, T. A. Trabold, Water management studies in pem fuel cells, part i: Fuel cell design and in situ water distributions, International Journal of Hydrogen Energy 34 (2009) 3436–3444.

[15] X. Zhang, J. Yang, X. Ma, W. Chen, S. Shuai, W. Zhuge, Numerical investigation of water dynamics in a novel wettability gradient anode flow channel for proton exchange membrane fuel cells, International Journal of Energy Research 44 (2020) 10282–10294.

[16] X. Ma, X. Zhang, J. Yang, W. Zhuge, S. Shuai, Impact of gas diffusion layer spatial variation properties on water management and performance of pem fuel cells, Energy Conversion and Management 227 (2020) 113579.

[17] Z. Lu, S. Kandlikar, C. Rath, M. Grimm, W. Domigan, A. White, M. Hardbarger, J. Owejan, T. Trabold, Water management studies in pem fuel cells, part ii: Ex situ investigation of flow maldistribution, pressure drop and two-phase flow pattern in gas channels, International Journal of Hydrogen Energy 34 (2009) 3445–3456.

[18] Z. Lu, M. M. Daino, C. Rath, S. G. Kandlikar, Water management studies in pem fuel cells, part iii: Dynamic breakthrough and intermittent drainage characteristics from gdls with and without mpls, International Journal of Hydrogen Energy 35 (2010) 4222–4233.

[19] Z. Lu, C. Rath, G. Zhang, S. G. Kandlikar, Water management studies in pem fuel cells, part iv: Effects of channel surface wettability, geometry and orientation on the two-phase flow in parallel gas channels, international journal of hydrogen energy 36 (2011) 9864–9875.

[20] J. T. Gostick, M. W. Fowler, M. A. Ioannidis, M. D. Pritzker, Y. M. Volfkovich, A. Sakars, Capillary pressure and hydrophilic porosity in gas diffusion layers for polymer electrolyte fuel cells, Journal of power sources 156 (2006) 375–387.

[21] J. T. Gostick, M. A. Ioannidis, M. W. Fowler, M. D. Pritzker, Direct measurement of the capillary pressure characteristics of water–air–gas diffusion layer systems for pem fuel cells, Electrochemistry Communications 10 (2008) 1520–1523.

[22] J. T. Gostick, M. A. Ioannidis, M. W. Fowler, M. D. Pritzker, Wettability and capillary behavior of fibrous gas diffusion media for polymer electrolyte membrane fuel cells, Journal of Power Sources 194 (2009) 433–444.

[23] I. Harkness, N. Hussain, L. Smith, J. Sharman, The use of a novel water porosimeter to predict the water handling behaviour of gas diffusion media used in polymer electrolyte fuel cells, Journal of Power Sources 193 (2009) 122–129.

[24] J. D. Fairweather, P. Cheung, J. St-Pierre, D. T. Schwartz, A microflu-

idic approach for measuring capillary pressure in pemfc gas diffusion layers, Electrochemistry Communications 9 (2007) 2340–2345.

[25] L. Hao, P. Cheng, Capillary pressures in carbon paper gas diffusion layers having hydrophilic and hydrophobic pores, International Journal of Heat and Mass Transfer 55 (2012) 133–139.

[26] Z. Niu, Y. Wang, K. Jiao, J. Wu, Two-phase flow dynamics in the gas diffusion layer of proton exchange membrane fuel cells: volume of fluid modeling and comparison with experiment, Journal of The Electrochemical Society 165 (2018) F613–F620.

[27] Z. Niu, Z. Bao, J. Wu, Y. Wang, K. Jiao, Two-phase flow in the mixed-wettability gas diffusion layer of proton exchange membrane fuel cells, Applied energy 232 (2018) 443–450.

[28] P. K. Sinha, C.-Y. Wang, Liquid water transport in a mixed-wet gas diffusion layer of a polymer electrolyte fuel cell, Chemical Engineering Science 63 (2008) 1081–1091.

[29] Q. Li, K. H. Luo, Q. Kang, Y. He, Q. Chen, Q. Liu, Lattice boltzmann methods for multiphase flow and phase-change heat transfer, Progress in Energy and Combustion Science 52 (2016) 62–105.

[30] Q. Li, Y. Yu, K. H. Luo, Implementation of contact angles in pseudopotential lattice boltzmann simulations with curved boundaries, Phys. Rev. E 100 (2019) 053313.

[31] L. Fei, K. H. Luo, C. Lin, Q. Li, Modeling incompressible thermal flows using a central-moments-based lattice boltzmann method, International Journal of Heat and Mass Transfer 120 (2018) 624–634.

[32] L. Fei, A. Scagliarini, A. Montessori, M. Lauricella, S. Succi, K. H. Luo, Mesoscopic model for soft flowing systems with tunable viscosity ratio, Physical Review Fluids 3 (2018) 104304.

[33] G. Molaeimanesh, M. Akbari, Impact of ptfe distribution on the removal of liquid water from a pemfc electrode by lattice boltzmann method, International journal of hydrogen energy 39 (2014) 8401–8409.

[34] J. Yu, D. Froning, U. Reimer, W. Lehnert, Apparent contact angles of liquid water droplet breaking through a gas diffusion layer of polymer electrolyte membrane fuel cell, International Journal of Hydrogen Energy 43 (2018) 6318–6330.

[35] G. Molaeimanesh, H. S. Googarchin, A. Q. Moqaddam, Lattice boltzmann simulation of proton exchange membrane fuel cells–a review on opportunities and challenges, International Journal of Hydrogen Energy 41 (2016) 22221–22245.

[36] B. Han, H. Meng, Numerical studies of interfacial phenomena in liquid water transport in polymer electrolyte membrane fuel cells using the lattice boltzmann method, International journal of hydrogen energy 38 (2013) 5053–5059.

[37] A. K. Gunstensen, D. H. Rothman, S. Zaleski, G. Zanetti, Lattice boltzmann model of immiscible fluids, Physical Review A 43 (1991) 4320.

[38] X. Shan, H. Chen, Lattice boltzmann model for simulating flows with multiple phases and components, Physical Review E 47 (1993) 1815.

[39] X. Shan, H. Chen, Simulation of nonideal gases and liquid-gas phase transitions by the lattice boltzmann equation, Physical Review E 49 (1994) 2941.

[40] M. R. Swift, W. Osborn, J. Yeomans, Lattice boltzmann simulation of nonideal fluids, Physical review letters 75 (1995) 830.

[41] X. He, S. Chen, R. Zhang, A lattice boltzmann scheme for incompressible multiphase flow and its application in simulation of rayleigh–taylor instability, Journal of computational physics 152 (1999) 642–663.

[42] L. Hao, P. Cheng, Lattice boltzmann simulations of water transport in gas diffusion layer of a polymer electrolyte membrane fuel cell, Journal of Power Sources 195 (2010) 3870–3881.

[43] G. Molaeimanesh, M. Akbari, Role of wettability and water droplet size during water removal from a pemfc gdl by lattice boltzmann method, International Journal of Hydrogen Energy 41 (2016) 14872–14884.

[44] W. Chen, F. Jiang, Impact of ptfe content and distribution on liquid–gas flow in pemfc carbon paper gas distribution layer: 3d lattice boltzmann

simulations, international journal of hydrogen energy 41 (2016) 8550–8562.

[45] J. Yu, D. Froning, U. Reimer, W. Lehnert, Polytetrafluorethylene effects on liquid water flowing through the gas diffusion layer of polymer electrolyte membrane fuel cells, Journal of Power Sources 438 (2019) 226975.

[46] H. Deng, Y. Hou, K. Jiao, Lattice boltzmann simulation of liquid water transport inside and at interface of gas diffusion and micro-porous layers of pem fuel cells, International Journal of Heat and Mass Transfer 140 (2019) 1074–1090.

[47] R. Flückiger, F. Marone, M. Stampanoni, A. Wokaun, F. N. Büchi, Investigation of liquid water in gas diffusion layers of polymer electrolyte fuel cells using x-ray tomographic microscopy, Electrochimica Acta 56 (2011) 2254–2262.

[48] R. Lenormand, E. Touboul, C. Zarcone, Numerical models and experiments on immiscible displacements in porous media, Journal of fluid mechanics 189 (1988) 165–187.

[49] P. P. Mukherjee, C.-Y. Wang, Q. Kang, Mesoscopic modeling of two-phase behavior and flooding phenomena in polymer electrolyte fuel cells, Electrochimica Acta 54 (2009) 6861–6875.

[50] X.-D. Niu, T. Munekata, S.-A. Hyodo, K. Suga, An investigation of water-gas transport processes in the gas-diffusion-layer of a pem fuel cell by a multiphase multiple-relaxation-time lattice boltzmann model, Journal of Power Sources 172 (2007) 542–552.

[51] Y. Tabe, Y. Lee, T. Chikahisa, M. Kozakai, Numerical simulation of liquid water and gas flow in a channel and a simplified gas diffusion layer model of polymer electrolyte membrane fuel cells using the lattice boltzmann method, Journal of Power Sources 193 (2009) 24–31.

[52] S. Sakaida, Y. Tabe, T. Chikahisa, Large scale simulation of liquid water transport in a gas diffusion layer of polymer electrolyte membrane fuel cells using the lattice boltzmann method, Journal of Power Sources 361 (2017) 133–143.

[53] L. Fei, J. Du, K. H. Luo, S. Succi, M. Lauricella, A. Montessori, Q. Wang, Modeling realistic multiphase flows using a non-orthogonal multiple-relaxation-time lattice boltzmann method, Physics of Fluids 31 (2019) 042105.

[54] J. Yang, X. Ma, L. Fei, X. Zhang, K. H. Luo, S. Shuai, Effects of hysteresis window on contact angle hysteresis behaviour at large bond number, Journal of Colloid and Interface Science (2020).

[55] J. Yang, K. H. Luo, X. Ma, Y. Li, S. Shuai, Effects of perforation shapes on water transport in pemfc gas diffusion layers, SAE International

Journal of Advances and Current Practices in Mobility 1 (2019) 808–814. 2019-01-0380.

[56] L. Fei, J. Yang, Y. Chen, H. Mo, K. H. Luo, Mesoscopic simulation of three-dimensional pool boiling based on a phase-change cascaded lattice boltzmann method, Physics of Fluids 32 (2020) 103312.

[57] Z. Guo, C. Zheng, B. Shi, Discrete lattice effects on the forcing term in the lattice boltzmann method, Physical Review E 65 (2002) 046308.

[58] D. d'Humieres, Multiple–relaxation–time lattice boltzmann models in three dimensions, Philosophical Transactions of the Royal Society of London. Series A: Mathematical, Physical and Engineering Sciences 360 (2002) 437–451.

[59] L. Fei, K. H. Luo, Q. Li, Three-dimensional cascaded lattice boltzmann method: Improved implementation and consistent forcing scheme, Physical Review E 97 (2018) 053309.

[60] Q. Li, D. Du, L. Fei, K. H. Luo, Three-dimensional non-orthogonal mrt pseudopotential lattice boltzmann model for multiphase flows, Computers &. Fluids 186 (2019) 128 – 140.

[61] P. Yuan, L. Schaefer, Equations of state in a lattice boltzmann model, Physics of Fluids 18 (2006) 042101.

[62] C. E. Colosqui, G. Falcucci, S. Ubertini, S. Succi, Mesoscopic simulation

of non-ideal fluids with self-tuning of the equation of state, Soft matter 8 (2012) 3798–3809.

[63] Q. Li, K. H. Luo, Q. Kang, Q. Chen, Contact angles in the pseudopotential lattice boltzmann modeling of wetting, Physical Review E 90 (2014) 053301.

[64] A. Nabovati, J. Hinebaugh, A. Bazylak, C. H. Amon, Effect of porosity heterogeneity on the permeability and tortuosity of gas diffusion layers in polymer electrolyte membrane fuel cells, Journal of Power Sources 248 (2014) 83–90.

[65] M. Shojaeefard, G. Molaeimanesh, M. Nazemian, M. Moqaddari, A review on microstructure reconstruction of pem fuel cells porous electrodes for pore scale simulation, International Journal of Hydrogen Energy 41 (2016) 20276–20293.

[66] Z. Fishman, A. Bazylak, Heterogeneous through-plane porosity distributions for treated pemfc gdls i. ptfe effect, Journal of the Electrochemical Society 158 (2011) B841–B845.

[67] J. Benziger, J. Nehlsen, D. Blackwell, T. Brennan, J. Itescu, Water flow in the gas diffusion layer of pem fuel cells, Journal of Membrane Science 261 (2005) 98–106.

[68] Y. Wang, S. Cho, R. Thiedmann, V. Schmidt, W. Lehnert, X. Feng, Stochastic modeling and direct simulation of the diffusion media for

polymer electrolyte fuel cells, International journal of heat and mass transfer 53 (2010) 1128–1138.